

Article

Cross-Subject EEG Channel Selection Method for Lower Limb Brain-Computer Interface

Mingnan Wei^{1,2}, Mengjie Huang^{3,*}, and Jiaying Ni³¹ School of Advanced Technology, Xi'an Jiaotong-Liverpool University, Suzhou, 215123, China² Department of Computer Science, University of Liverpool, Liverpool, L69 3BX, United Kingdom³ Design School, Xi'an Jiaotong-Liverpool University, Suzhou, 215123, China* Correspondence: Mengjie.Huang@xjtlu.edu.cn

Received: 27 April 2023

Accepted: 30 June 2023

Published: 26 September 2023

Abstract: Lower limb motor imagery (MI) classification is a challenging research topic in the area of brain-computer interfaces (BCIs), and entails numerous signal channels to provide sufficient information about the background neural activity. However, practical applications often lack the environment to accommodate excessive channels due to the time-consuming setup process, inconvenient movement, and restricted application scenarios. The existing channel selection algorithms (designed for the individual subject) place a great deal of focus on the classified performance comparisons, whereas the significance of actual locations and neural functions of brain regions is disregarded. Although these algorithms require significant computation resources, their selected solutions cannot be re-used for other subjects to realize the cross-subject channel selection and improve the reusability of model due to poor interpretability and inapplicability. To date, there have been no investigations about the cross-subject channel selection problem for the lower limb MI stepping tasks. This study proposes an optimal cross-subject lower limb channel selection that selectively retains significant channels, narrows the computation scope of the selection, and obtains the optimal selection solutions. Through stepping-based MI experiments, the proposed optimal channel selection enables effective recognition in low-channel settings, thereby contributing a lot to the development of generic and convenient lower limb BCI systems. Additionally, statistical analysis reveals a significant difference in energy spectrum between left and right stepping-based MI tasks in the θ and μ bands of the frontal lobe channels, providing new evidence that the frontal lobe dramatically affects lower limb MI tasks.

Keywords: brain-computer interface; motor imagery; channel selection; cross-subject; deep transfer learning

1. Introduction

The brain-computer interface (BCI) is a promising technology that decodes brain signals with the purpose of classification, decision-making, instruction-delivering and device-controlling [1–3]. Motor imagery (MI) based BCI systems can help subjects manipulate the devices by imaging the movements and evoking the brain activity, and have been widely used in rehabilitation and auxiliary engineering to restore or replace impaired communication or motor functions [4–8]. Since the physiological MI representation areas (for the left and right lower limbs) locate within the interhemispheric fissure (of the sensorimotor cortex) and share the proximity spatially, MI classification for lower limb movements has been a challenging research topic in the BCI field [9–11].

Currently, the evolution of wearable sensor technologies and mobile electroencephalography (EEG) systems has built a bridge between laboratory-oriented BCI experiments and real-world applications [12–16]. To obtain high-performance lower limb BCIs, the study needs numerous EEG channels to provide sufficient information about the neural activity in the background, resulting in exorbitant measurement costs and uncomfortable user experiences [16–17]. In addition, to optimize the use of channels, it is essential to have an environment that allows for convenient usage of sufficient channels at most of the time. However, in tasks such as lower limb exoskeleton stepping or virtual reality games, excessive channels can lead to longer setup times, restricted movements, and limited application scenarios when subjects wear EEG caps. Furthermore, superfluous channels can exacerbate overfitting effects, increase compu-

tational loads, and weaken the interpretability of the system [16]. Removing irrelevant and low-value channels can also help reduce the redundancy of classified information and improve classification accuracy. Given the limited number of channels caused by the limitation of objective conditions, it is crucial to design an optimal solution with the minimal channels and maintain an efficient classification performance for the lower limb BCI to be translated into daily use.

The channel selection algorithm is the primary method to solve the selection issue. In lower limb MI classification, channels are typically selected to determine the best channels by comparing their contributions to MI detection or the mutual information of channel correlations. Gurve et al. utilized neighborhood component analysis and non-negative matrix factorization to extract the contribution weight of EEG channels and select subject-specific features [18]. This channel selection method for relaxing-pedaling MI-BCIs results in the improvement of 13.20% in detection accuracy and the improvement of 27% in the Kappa value. Gaur et al. computed the correlation between EEG signals for a particular subject, and selected highly correlated EEG channels based on the Pearson correlation coefficient [19]. For public datasets with the left/right hand and foot imagined tasks, a minimum number of EEG channels are identified with the average channel reduction of 65.45%, and an increase over 5% is demonstrated in accuracy using the channel Cz as a reference.

There are also some challenges to deal with, although current lower limb MI channel selection algorithms can simplify the EEG acquisition process. Firstly, existing channel selection algorithms are designed for a single subject, which cannot be reused for multiple subjects. This lack of generalization is an extra burden for data re-collection and model re-training. It would be valuable for widely applied EEG systems if the channel selection algorithm could be reused for multiple subjects to avoid duplicative work. Secondly, the algorithms focus excessively on the classified performance and ignore the significance of the actual locations or neural functions of brain regions, leading to solutions with poor interpretability. Adopting the anatomy and cognitive neural information of the brain as prior knowledge can significantly narrow the computation scope of the channel selection and avoid the comparison of all subsets. Therefore, the channel selection under limited channel numbers should consider the cognitive neural effects of brain regions rather than the pure results of a single experiment.

Based on the analysis above, this paper investigates channel selection algorithms for lower limb MI classification. To the authors' best knowledge, no research has discussed the channel selection problem for cross-subject lower limb MI classification. Furthermore, it is necessary to overcome the challenge that, the existing lower limb MI channel selection algorithms have paid no attention to the influences of actual brain functions. Facing the challenges in both subject specificity and performance interpretability, an optimal cross-subject lower limb channel selection for MI tasks is proposed by combining the functions of brain regions and the classified results, in order to simplify the acquisition process and provide generic and interpretable solutions. By selectively retaining the channels in the most relevant region of the MI task, the optimal channel selection can be directly applied to the cross-subject lower limb MI classification scheme for the recognition of multiple subjects. Therefore, finding the optimal channel selection is significantly beneficial in constructing convenient and generic BCIs for multiple users.

Considering the lower limb MI channel selection problem under limited channel numbers, the main contributions of this paper are summarized as follows:

- 1) By adopting physiological brain functions and selectively reserving channels in the most MI-relevant region, an optimal cross-subject lower limb channel selection for MI classification is proposed to achieve multi-user reutilization and reduce computational costs.
- 2) The proposed channel selection is successfully verified in the analysis of cross-subject lower limb stepping-based MI experiments, where the performance is proved to be efficient for different classifiers.
- 3) A significant energy spectrum difference between left and right stepping-based MI tasks is observed in θ and μ bands of the frontal lobe channels. These new findings demonstrate that the frontal lobe plays a significant role in lower limb MI classification and can serve as a basis for further development of generic lower limb BCIs.

The rest of this paper is organized as follows. Section 2 describes the design of the stepping-based MI experiments and the proposed optimal channel selection for the stepping-based MI classification scheme. Section 3 presents the detailed experimental results of the proposed methods and discusses the statistical analysis of the frontal lobe channels. Finally, Section 4 concludes this paper and discusses future work.

2. Materials and Methods

This section begins by introducing the stepping-based MI signal acquisition experiments including the experimental subjects, site, apparatus, and tasks. Next, the decision-based cross-subject lower limb channel selection and the stepping-based MI classification scheme are presented in detail.

2.1. EEG Data Acquisition

2.1.1. Ethics

This research has been approved by University Ethics Committee of Xi'an Jiaotong-Liverpool University with decision number EXT20-01-07 on March 31 2020. Prior to the experiments, the subjects read, and when they agreed, signed the consent form prior approved by the University Ethics Committee of Xi'an Jiaotong-Liverpool University.

2.1.2. Subjects

Six healthy subjects (two males and four females aged 22-35 years) participated in the experiments with no history of lower limb injuries or reported neurological deficiencies. The experimental protocol has been approved by the local research ethics committee, and all participants provided informed consent after receiving a detailed explanation of the procedure.

2.1.3. Experiment Site

The experiment is conducted in a specially designed electromagnetic isolation lab (as shown in [Figure 1](#)) surrounded by metal isolation walls and ceilings to minimize noises and electromagnetic disturbances. The internal power supply and lighting are filtered to prevent the interference from power signals.

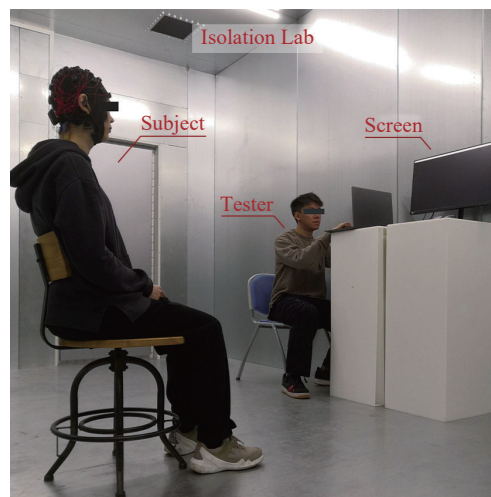


Figure 1. Experiment setup in electromagnetic isolation lab.

2.1.4. Saline Electrode Apparatus and Settings

In this study, EEG data is collected using a 32-electrode headcap (Emotiv EPOC Flex Saline Kit), and the Bluetooth technology is used to facilitate the real-time data collection and transmission to a computer. The electrode placement follows the international 10-20 system [20] with electrodes located at FP1, FP2, F3, F4, F7, F8, FC1, FC2, FC3, FC4, FC5, FC6, Cz, C1, C2, C3, C4, CP1, CP2, CP3, CP4, CP5, CP6, Pz, P1, P2, P3, P4, POz, O1, Oz, and O2, as illustrated in [Figure 2\(a\)](#). Additionally, the reference electrodes are positioned at the mastoid locations TP9 and TP10 on both sides. EEG data is collected continuously at a sampling rate of 128 Hz throughout the experiment.

2.1.5. Gel Electrode Apparatus and Settings

In this study, an EEG headcap (Emotiv EPOC Flex Gel Kit) is employed using the gel as the electrode-cortex medium. Different from the previous one using saline, this experiment utilizes 18 channels including FPz, FP1, FP2, FCz, FC1, FC2, FC3, FC4, Cz, C1, C2, C3, C4, CPz, CP1, CP2, CP3, and CP4, as depicted in [Figure 2\(b\)](#). The reference electrodes are positioned at the bilateral earlobes A1 and A2, and the headcap is sampled at a rate of 128 Hz.

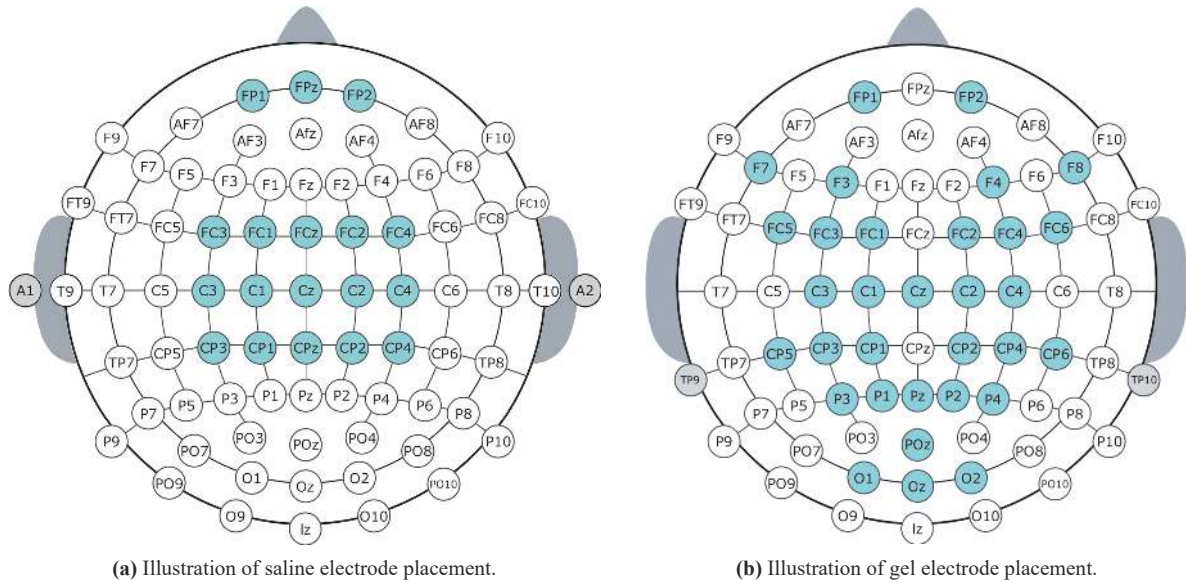


Figure 2. Illustration of gel and saline electrode placement (in blue/grey circles).

2.1.6. Motor Imagery Tasks

In the experimental paradigms (as shown in Figure 3), each trial lasts 12 seconds and commences with a fixation cross displayed on the screen for 3 seconds so as to prompt the participant to focus their attention. Subsequently, a random visual cue is presented with a right or left arrow to indicate the direction of the stepping-based MI task. The visual cues are displayed for 1 second, followed by an 8-second blank screen during which the MI task is performed. An audio beep sound ends the task, followed by a short rest period lasting 4-8 seconds (which is adjustable according to the subject's completion and fatigue status). Each subject performs multiple iterations of the stepping-based MI tasks. For subsequent analysis, a total of 40 and 80 valid trials are completed by each participant in the gel and saline electrode experiments, respectively.

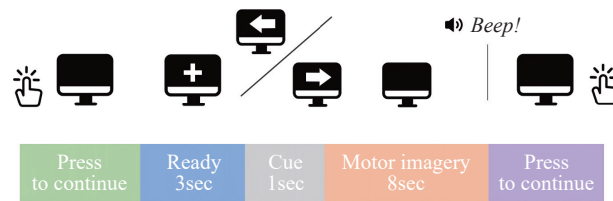


Figure 3. Temporal sequence of a stepping-based motor imagery (MI) trial.

2.2. Stepping-Based MI Classification Scheme

2.2.1. Scheme Overview

As shown in Figure 4, the stepping-based MI classification scheme consists of five main components: channel selection, data preprocessing, data alignment, feature extraction, and feature classification. In addition to the proposed optimal channel selection, this scheme incorporates bandpass filtering, independent component analysis (ICA), euclidean alignment (EA), multi-band common spatial pattern (MBCSP), and deep transfer learning (DTL) techniques.

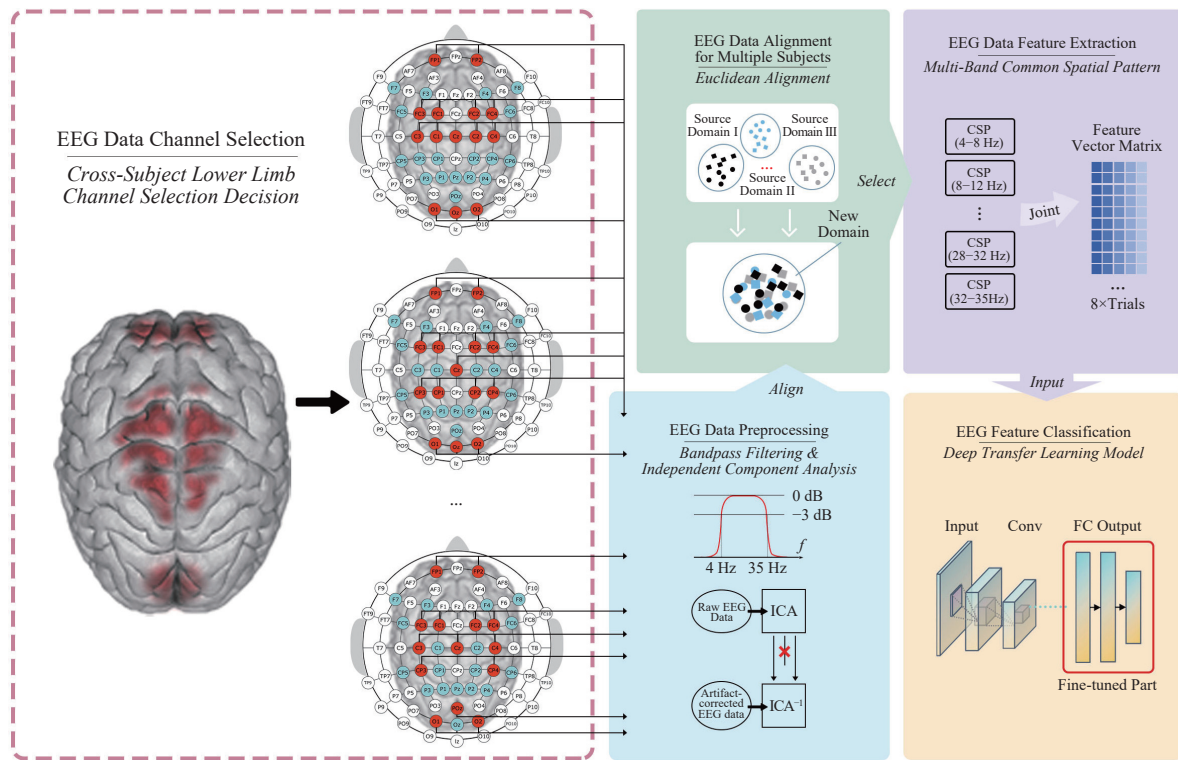


Figure 4. Cross-subject lower limb motor imagery (MI) classification scheme.

2.2.2. Cross-Subject Lower Limb Channel Selection

To determine the most relevant channels for stepping-based MI tasks, the effects of different brain regions are taken into account in the channel selection based on the anatomy and cognitive neural research. Given that the lower limb movement representation areas are primarily located in the central area of the mantelkante (the deep region inside the interhemispheric fissure), central area channels are crucial for lower limb MI classification tasks [11, 21–22]. Furthermore, the frontal lobe plays a significant role in limb movements (with most of the fibers related to such movements originating in this area), and is also closely associated with attention, memory, problem-solving, and other advanced cognitive functions [23–24]. Imagery of movements during MI tasks involves the visual cortex of the occipital lobe, which is responsible for processing language, motor sensation, abstract concepts, and visual information [25]. Therefore, front and occipital lobe channels can be considered supplementary for MI classification tasks [21, 26].

To address the challenges of lower limb MI classification for multiple subjects with limited channels, this study proposes an optimal cross-subject lower limb channel selection based on the prior knowledge of functional brain areas. The specific procedure is illustrated in Figure 5 by retaining central, frontal, and occipital lobe channels as the primary elements, while preferentially removing channels exactly (or approximately) located in low-impact brain regions. The selection process considers the collaborative and complementary effects of multi-brain regions rather than solely retain the most significant area. The use of the prior knowledge narrows the computation scope of the selection and thus, exhaustive performance comparisons are conducted to obtain the optimal solutions under the required channel number. Furthermore, detailed and comprehensive statistics are carried out in multiple classifiers to verify the consistency of the optimal selection solutions. The decision simplifies EEG signal acquisition and enables efficient cross-subject lower limb MI classification by retaining the most valuable brain region channels for the subjects, minimizing the practical channel number, and maintaining the optimal classification accuracy.

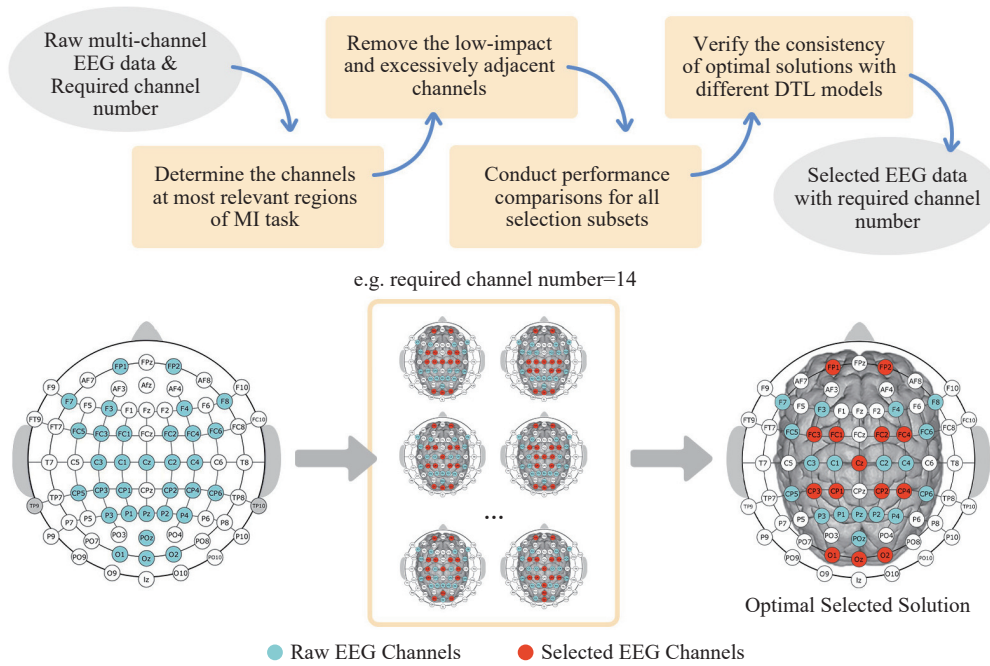


Figure 5. Procedure of cross-subject lower limb channel selection.

2.2.3. Bandpass Filtering & Independent Component Analysis

The data preprocessing techniques such as bandpass filtering and ICA decomposition are implemented using the EEGLAB toolbox [27]. The pre-processing methods aim to eliminate outliers and artifacts in the data including both physiological artifacts (such as electrocardiograph, electromyography, and electrooculography) and non-physiological artifacts (such as the powerline interference, poor electrode contact with the scalp, and impedance fluctuations). As the bandpass filter allows waves in a specific band to pass through and blocks other bands [28–29], the bandpass filtering in this scheme retains 4-35 Hz signals ($\theta + \mu + \beta$), where most MI characteristic information is contained and the signals (such as noises of power frequency 50-60 Hz, motion-induced artifacts, skin artifacts at low frequencies, and artifacts caused by sweating) are eliminated.

Following bandpass filtering, ICA decomposes the multi-channel EEG into many statistically independent components for removal. ICA is a blind source separation algorithm that can separate statistically independent components from collected multi-channel EEG data [30]. As each EEG channel records the difference between the reference channel potential and the combined potential (generated by sources at different brain locations which are projected into the channel), the ICA algorithm decomposes multi-channel EEG signals by using linear transformation to obtain multiple corresponding independent components that are projected from different positions.

2.2.4. Euclidean Alignment

EA is an unsupervised distributed adaptation method to align data between different subjects [31]. In this technique, EEG signals from multiple subjects are mapped to a new space to minimize the difference in the average data covariance and ensure the consistent data distribution. The concepts adopted in EA are explained in this subsection and the notations are shown in Table 1. Given the EEG signal matrix $X \in \mathbb{R}^{N \times P}$ with the channel number N and the sampling point number P , the first thing is to calculate the reference matrix \bar{E} (the Euclidean mean of all EEG trials) for each subject's data as shown in Equation (1).

Table 1 Notations in Euclidean alignment in the paper

Notation	Description
\bar{E}	the reference matrix
i	the current trial number
n	the total quantityd of trials
N	the channel numbers
P	the sampling point number
T	the transposition symbol
X	the EEG matrix
\bar{X}	the aligned EEG matrix

$$\bar{E} = \frac{1}{n} \sum_{i=1}^n X_i X_i^T \quad (1)$$

where i is the current trial number, n is the total quantity of trials and T is the transposition symbol.

According to \bar{E} , EA is performed by mapping the EEG signals of each subject to a new space. The aligned EEG signal matrix \tilde{X} can be obtained as shown in Equation (2).

$$\tilde{X}_i = \bar{E}^{-1/2} X_i \quad (2)$$

where $i \in [1, n]$.

Through EA, the mean covariance matrix is equal to the identity matrix and is used to form similar covariance matrix distributions for different subjects as shown in Equation (3).

$$\begin{aligned} \frac{1}{n} \sum_{i=1}^n \tilde{X}_i \tilde{X}_i^T &= \frac{1}{n} \sum_{i=1}^n \bar{E}^{-1/2} X_i X_i^T \bar{E}^{-1/2} \\ &= \bar{E}^{-1/2} \left(\frac{1}{n} \sum_{i=1}^n X_i X_i^T \right) \bar{E}^{-1/2} \\ &= \bar{E}^{-1/2} \bar{E} \bar{E}^{-1/2} = I \end{aligned} \quad (3)$$

In data alignment, EA is adopted to map the preprocessed data of multiple subjects into a new common domain, minimize their average covariance matrix difference, and generate the hybrid data as the extraction target.

2.2.5. Multi-Band Common Spatial Pattern

The MBCSP method, as described in [32], can effectively extract spatial distribution components of two classes from multiple sub-band signals, resulting in a feature vector with a high level of discrimination. The concepts adopted in MBCSP are explained in this subsection and the notations are shown in Table 2. To achieve the extraction, a raw EEG matrix $E \in \mathbb{R}^{N \times P}$ with N channels and P sampling points is filtered using a series of bandpass filters to produce multiple sub-band signals $E^{(i)}$. For each sub-band signal, the normalized covariance matrices for $R_1^{(i)}$, $R_2^{(i)}$ and $R^{(i)}$ are computed. Additionally, by applying the whitening transformation $P^{(i)}$ as shown in Equation (4), it is seen that the spanned space variances of the eigenvectors in $R^{(i)}$ are equal.

$$P^{(i)} = \sqrt{\Sigma^{-1}^{(i)}} U^{T(i)} \quad (4)$$

where T is the transpose symbol, $U^{(i)}$ is the eigenvector matrix of the sub-band i , and Σ is the diagonal matrix of eigenvalues (the eigenvalues are assumed to be sorted in descending order). The transformed matrices S_1 and S_2 of R_1 and R_2 are displayed in Equation (5).

$$S_{1,2}^{(i)} = P^{(i)} R_{1,2}^{(i)} P^{T(i)} \quad (5)$$

where $S_1^{(i)}$ and $S_2^{(i)}$ share the same eigenvectors.

Table 2 Notations in multi-band common spatial pattern in the paper

Notation	Description
B	the eigenvector matrix
E	the raw EEG matrix
i	the sub-band number
I	the identity matrix
m	the quantity of chosen lines
N	the channel number
P	the sampling point number
R	the normalized covariance matrix
S	the transformed matrix
T	the transposition symbol
U	the eigenvector matrix
W	the projection matrix
W'	the screening projection matrix
Z	the projected matrix
Σ	the diagonal matrix of eigenvalues
f	the extracted features

The principal component decomposition can decompose both $S_1^{(i)}$ and $S_2^{(i)}$ using the same eigenvector matrix, resulting in the sum of corresponding eigenvalues being equal to one, as illustrated in Equation (6):

$$S_{1,2}^{(i)} = B^{(i)} \Sigma_{1,2}^{(i)} B^{T(i)}, \Sigma_1^{(i)} + \Sigma_2^{(i)} = I \quad (6)$$

where $B^{(i)}$ is the eigenvector matrix, $\Sigma_1^{(i)}$ and $\Sigma_2^{(i)}$ are the diagonal matrices (consisting of eigenvalues) for the two classes of data, and I is the identity matrix.

Since the eigenvector (corresponding to the maximum eigenvalue of $S_1^{(i)}$) minimizes the eigenvalue of $S_2^{(i)}$, and vice versa, the difference between the two classes' signals is maximized. As a result, the projection matrix of the spatial filter $W^{(i)}$ can be obtained in Equation (7):

$$W^{(i)} = B^{T(i)} P^{(i)} \quad (7)$$

The maximum and minimum eigenvalues of $W^{(i)}$ are presented in the first and last rows of the eigenvalue matrix followed by the descending order of the matrix. Consequently, the screening projection matrix $W'^{(i)}$ is created using the first m rows and the last m rows of W . The projected matrix $Z^{(i)}$ can be obtained by filtering $E^{(i)}$ with $W'^{(i)}$ as shown in Equation (8):

$$Z^{(i)} = W'^{(i)} E^{(i)} \quad (8)$$

The features $f^{(i)}$ that maximize the difference in variances of two classes are defined below:

$$f^{(i)} = \log \left(\frac{\text{var}(Z^{(i)})}{\sum_{n=1}^{2m} \text{var}(Z_n^{(i)})} \right) \quad (9)$$

where the value of m is typically 1, and the aggregated features are obtained by combining $f^{(i)}$ of all sub-bands in series.

The stepping-based MI classification scheme utilizes MBCSP to split the hybrid data, ranging from 4 Hz to 35 Hz, into multiple 4 Hz interval sub-bands. After the spatial extraction of each sub-band, the resultant features are combined to form aggregated features for classified information aggregation.

2.2.6. Deep Transfer Learning Classifier

In the last decade, deep learning has undoubtedly been one of the most scrutinized studies in engineering and has been successfully applied to many real-world applications. Deep learning algorithms can automatically learn high-level features from massive data by utilizing the unsupervised or semi-supervised feature learning algorithms as well as the hierarchical feature extraction technique, resulting in the performance which far exceeds that of the traditional methods in most cases [33–34]. Since deep learning is a representation learning algorithm based on large-scale data, data dependency is one of the most severe problems which limits the model performance [33]. Transfer learning is an essential tool in machine learning to solve the fundamental problem of insufficient training data. The DTL method refers to the deployment of deep learning for transfer learning, which transfers potentially transferable knowledge from other fields (source domains) into the target field (the target domain) [35–37]. DTL can significantly reduce the demand for training data and training time in the target domain, thereby solving the problem of insufficient training data [38–40].

Network-based DTL is a suitable and effective approach to the target domains of small datasets such as EEG data. Since the front layers of the network can be treated as a versatile feature extractor, the network-based DTL refers to reuse the partial layers of a pre-trained network (trained by massive data in the source domain), including its network structure and connection parameters which are later transferred to a part of the pre-trained network used in the target domain. Since the pre-trained network has already learned to extract informative and robust features, the new model can achieve high-performance classification only by fine-tuning and updating the transferred sub-network based on a small amount of data in the target domain [41]. The convolutional neural network (CNN), as a category of outstanding models with typical significance in deep learning, is often used as the target of transfer learning [42–45]. Due to the weight-sharing feature, the CNN reduces the number of trainable network parameters, which helps the network to enhance generalization and avoid overfitting. Moreover, concurrently learning the feature extraction and classification layers results in the fact that the model output is high-organized and high-reliant on the features. Therefore, the CNN is suitably used for implementing knowledge transferring of large-scale network implementation.

A pre-trained CNN-based DTL is used as the final classifier in the scheme to improve the classification performance and save retraining costs [46–52]. The spatial features are first converted into grayscale images and later colored using a pseudo-color tool. These feature images are then rescaled into the required pixels of the DTL classifier. The fine-tuned method rebuilds the last fully-connected layers of the network and adjusts the weights using the feature images.

3. Results and Analysis

In this study, a range of CNNs (including the AlexNet, GoogLeNet, VGG16, VGG19, ResNet-18, ResNet-50, ResNet-101, Inception-v3, and DenseNet-201 [53–56]) are employed to verify the consistency of the proposed optimal results via several model performance comparisons. The programming language used is Matlab, and the hardware specifications are: Intel Xeon CPU E5-2678 v3, Nvidia GeForce Titan RTX GPU with 24 GB of memory, and 64 GB of RAM.

With different available channel numbers, the performances of cross-subject lower limb MI classification schemes are displayed in Figure 6 and Figure 7 for the saline and gel electrode data, respectively. Figure 6 presents a comparison of the classification accuracy achieved by the cross-subject schemes on the saline and gel electrode data. The results indicate that schemes utilizing light-weighted DTL classifiers outperform those using complex structures. Additionally, the schemes adopting AlexNet, VGG16, and VGG19 consistently achieve the highest accuracy across all channel selection solutions.

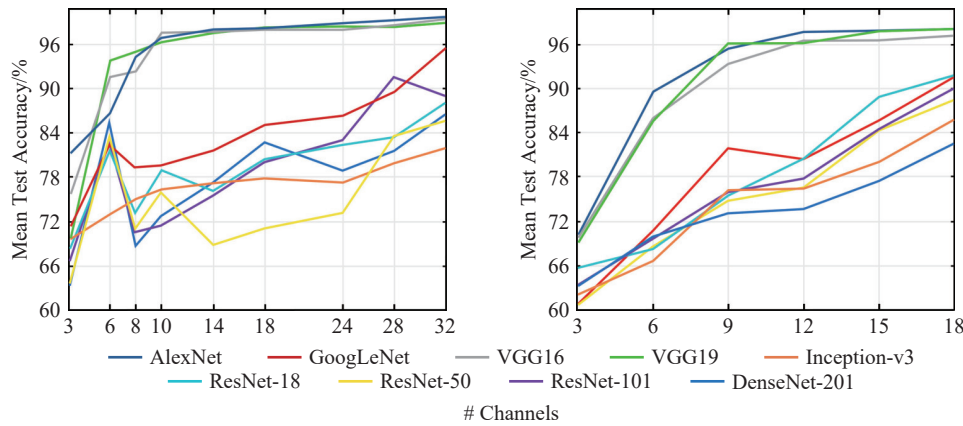


Figure 6. Comparison of the cross-subject schemes using different DTL classifiers and data from both saline and gel electrodes. Mean test accuracies across the subjects are plotted against the number of selection neurons.

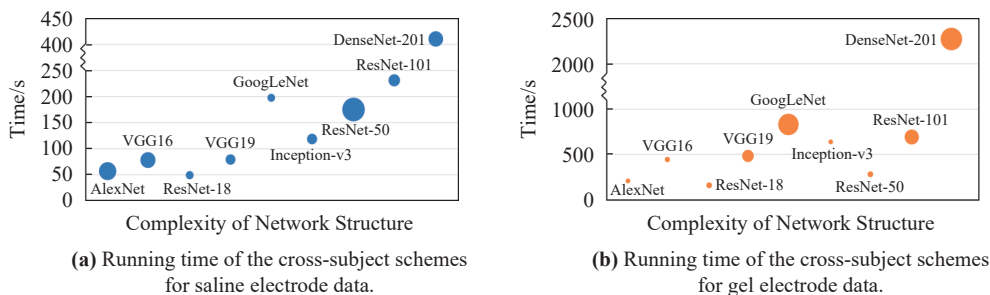


Figure 7. Running time of the cross-subject schemes using various DTL classifiers. According to the structure complexities, networks are sorted in ascending order from left to right.

The AlexNet scheme achieves the highest accuracy of $99.0 \pm 0.7\%$ and $97.8 \pm 1.3\%$ in the saline and gel electrode experiments, respectively. Although there is a slight decline in accuracy as the available channel number decreases, the cross-subject schemes are still able to achieve successful classification based on the optimal channel selections. For instance, when the channel number is reduced from 32 to 6 in the saline electrode experiments, the majority of schemes retain high-performance classification abilities and reach accuracy above 80%. Remarkably, the VGG16 and VGG19 schemes always achieve cross-subject classification with more than 90% accuracy. When the channel number is reduced from 18 to 9 in the gel electrode experiments, most schemes can maintain accuracy above 72%, whereas the schemes using AlexNet, VGG16, and VGG19 obtain accuracy above 93%. Even when only three channels are used, the AlexNet schemes can still achieve 81.4% and 70.3% accuracy in the saline and gel electrode experiments, respectively.

Figure 7 presents the running time of the schemes on saline and gel electrode data. The horizontal and vertical axes represent the complexity of the network structure and the running time of the cross-subject schemes, respectively. The schemes are sorted from left to right based on the increase in structure complexity. All schemes are symbolized with circles, where the diameter represents the range of running time of the network. Notably, the schemes with AlexNet, VGG16, and ResNet-18 require less time for model training than those with complicated networks. Hence, the accuracy and running time results suggest that the light-weighted DTL classifiers could perform excep-

tionally well in the classification of stepping-based MI tasks.

Table 3 presents the percentage decrease in accuracy (the performance loss) for the saline electrode apparatus in comparison to that of full 32 channels. The AlexNet, VGG16, and VGG19 schemes exhibit only a minor average performance loss ($\leq 3\%$) when the number of channels is reduced from 32 to 10. The performance loss results for the gel electrode apparatus are listed in Table 4. When the number of gel electrode channels is reduced by half (from 18 to 9), the average performance loss for the AlexNet, VGG16, and VGG19 schemes does not exceed 2%. Combined with the classification results in Figure 6, the proposed optimal cross-subject lower limb channel selection has demonstrated its efficiency in simplifying signal acquisition for stepping-based MI tasks by reducing the practical channel number while maintaining the excellent classification performance.

Table 3 Accuracies differences between the optimal channel selection solutions and the maximal channels (#32) performance for cross-subject saline electrode data. Performances of schemes with different DTL classifiers are also compared.

Channel	AlexNet	VGG16	ResNet-18	VGG19	GoogLeNet	Inception-v3	ResNet-50	ResNet-101	DenseNet-201
3	↓ 18.4±4.8%	↓ 23.4±4.7%	↓ 19.5±6.1%	↓ 29.4±3.8%	↓ 24.2±7.2%	↓ 12.3±5.2%	↓ 21.8±5.3%	↓ 19.6±4.6%	↓ 23.1±6.7%
6	↓ 13.1±3.3%	↓ 7.3±2.8%	↓ 6.6±2.9%	↓ 5.1±2.3%	↓ 13.1±5.6%	↓ 8.9±2.9%	↓ 2.1±1.4%	↓ 3.8±1.7%	↓ 1.4±1.9%
8	↓ 5.5±2.4%	↓ 6.9±3.3%	↓ 15.0±5.5%	↓ 3.8±2.9%	↓ 16.0±6.5%	↓ 6.7±3.1%	↓ 14.5±4.9%	↓ 15.7±6.6%	↓ 17.7±4.6%
10	↓ 2.8±1.7%	↓ 1.5±2.6%	↓ 9.3±3.8%	↓ 2.1±2.4%	↓ 16.0±5.7%	↓ 5.5±4.3%	↓ 9.8±3.0%	↓ 14.8±3.8%	↓ 14.0±3.1%
14	↓ 1.7±1.8%	↓ 1.3±1.8%	↓ 11.9±4.4%	↓ 1.1±1.7%	↓ 13.8±5.6%	↓ 4.7±3.5%	↓ 16.7±5.2%	↓ 11.2±3.7%	↓ 9.3±4.3%
18	↓ 1.6±1.5%	↓ 1.2±1.5%	↓ 7.6±2.1%	↓ 0.8±1.3%	↓ 10.5±4.1%	↓ 3.8±3.7%	↓ 14.6±3.7%	↓ 6.3±2.8%	↓ 3.8±4.2%
24	↓ 0.8±1.2%	↓ 1.2±1.3%	↓ 5.5±1.3%	↓ 0.6±1.5%	↓ 9.3±4.2%	↓ 4.6±2.5%	↓ 12.5±3.2%	↓ 3.5±2.7%	↓ 7.6±3.3%
28	↓ 0.5±0.9%	↓ 0.6±1.3%	↓ 4.7±1.2%	↓ 0.5±1.2%	↓ 5.6±3.7%	↓ 2.0±2.6%	↓ 2.1±2.5%	↑ 5.3±2.2%	↓ 5.1±3.5%

Table 4 Accuracy differences between the optimal channel selection solutions and the maximal channels (#18) performance for cross-subject gel electrode data. Performances of schemes with different DTL classifiers are also compared.

Channel	AlexNet	VGG16	ResNet-18	VGG19	GoogLeNet	Inception-v3	ResNet-50	ResNet-101	DenseNet-201
3	↓ 28.0±4.3%	↓ 27.4±5.4%	↓ 25.9±5.9%	↓ 29.0±5.8%	↓ 30.6±7.8%	↓ 23.7±6.8%	↓ 27.6±7.3%	↓ 26.5±7.8%	↓ 19.1±6.7%
6	↓ 8.6±3.1%	↓ 11.2±5.1%	↓ 23.3±7.6%	↓ 12.5±4.7%	↓ 20.7±6.9%	↓ 19.1±5.7%	↓ 19.7±8.1%	↓ 20.3±8.6%	↓ 12.6±6.8%
9	↓ 2.7±1.6%	↓ 3.9±1.5%	↓ 16.1±7.8%	↓ 2.0±1.4%	↓ 9.6±6.2%	↓ 9.6±4.3%	↓ 13.6±6.8%	↓ 13.9±4.1%	↓ 9.4±7.3%
12	↓ 0.5±1.1%	↓ 0.7±1.9%	↓ 11.2±4.5%	↓ 2.0±1.7%	↓ 11.0±6.7%	↓ 9.3±3.6%	↓ 11.8±6.2%	↓ 12.1±9.8%	↓ 8.8±2.4%
15	↓ 0.3±1.8%	↓ 0.6±1.2%	↓ 2.9±2.3%	↓ 0.4±1.1%	↓ 5.8±5.1%	↓ 5.7±3.1%	↓ 4.2±1.6%	↓ 5.5±3.2%	↓ 5.1±3.2%

Figure 8 displays the topographical maps of the optimal channel selection solutions for saline and gel electrode data. The adopted and unadopted channels under the current selected solutions are represented by red and blue colors, respectively. The results indicate that the optimal selection consistently retains most of the channels on the frontal lobe, central area, and occipital lobe. Additionally, the optimal solutions mainly adopt the frontal lobe channels. This highlights the substantial effects of the frontal lobe on lower limb MI stepping classification.

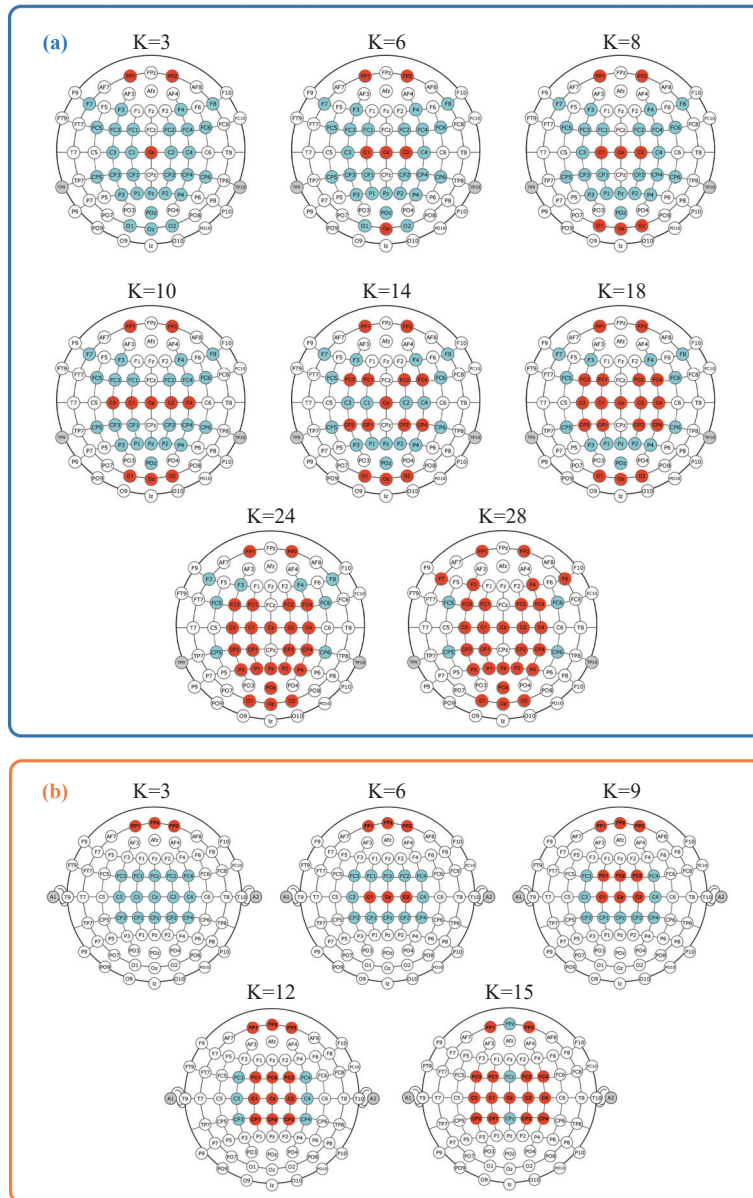


Figure 8. (a) Topographical maps of the optimal channel selection solutions for cross-subject saline electrode data. (b) Topographical maps of the optimal channel selection solutions for cross-subject gel electrode data. K is the channel number of the optimal channel selection solutions.

To investigate the influences of different brain regions on classification, the cross-subject scheme with the pre-trained AlexNet is adopted as the model due to its superior performance as detailedly shown in Tables 5 and 6. The results indicate that compared with other brain regions, the central area still significantly contributes to the classification of stepping-based MI tasks. Nevertheless, using six channels in the frontal lobe is only 4% less accurate than using 17 channels in the central area, and this highlights the profound effect of the frontal lobe on lower limb MI classification. Moreover, the synergistic and complementary effects of the frontal lobe area significantly improve the recognition accuracy of the schemes. When the frontal lobe channels are added to the schemes with central area channels, the accuracy increases from 84% to 97% and 88% to 97%, respectively. Similarly, adding frontal area channels to the parietal and occipital lobe channels increases the accuracy from 77% to 87%.

Table 5 Accuracies of the cross-subject schemes using pre-trained AlexNet and saline electrode data of each individual brain region

Brain Area	Numbers	Electrode Channels	Accuracies
Full placement	32	FP1, FP2, F3, F4, F7, F8, FC1, FC2, FC3, FC4, FC5, FC6, Cz, C1, C2, C3, C4, CP1, CP2, CP3, CP4, CP5, CP6, Pz, P1, P2, P3, P4, POz, O1, Oz, O2	99%
Frontal, parietal, occipital lobe	15	FP1, FP2, F3, F4, F7, F8, Pz, P1, P2, P3, P4, POz, O1, Oz, O2	89%
Central, parietal, occipital lobe	26	FC1, FC2, FC3, FC4, FC5, FC6, Cz, C1, C2, C3, C4, CP1, CP2, CP3, CP4, CP5, CP6, Pz, P1, P2, P3, P4, POz, O1, Oz, O2	87%
Frontal, central lobe	21	FP1, FP2, F3, F4, F7, F8, FC1, FC2, FC3, FC4, FC5, FC6, Cz, C1, C2, C3, C4, CP1, CP2, CP3, CP4	97%
Parietal, occipital lobe	9	Pz, P1, P2, P3, P4, POz, O1, Oz, O2	77%
Central lobe	17	FC1, FC2, FC3, FC4, FC5, FC6, Cz, C1, C2, C3, C4, CP1, CP2, CP3, CP4, CP5, CP6	84%
Frontal lobe	6	FP1, FP2, F3, F4, F7, F8	80%

Table 6 Accuracies of the cross-subject schemes using pre-trained AlexNet and gel electrode data of each individual brain region

Brain Area	Numbers	Electrode Channels	Accuracies
Full placement	18	FPz, FP1, FP2, FCz, FC1, FC2, FC3, FC4, Cz, C1, C2, C3, C4, CPz, CP1, CP2, CP3, CP4	97%
Central lobe	15	FCz, FC1, FC2, FC3, FC4, Cz, C1, C2, C3, C4, CPz, CP1, CP2, CP3, CP4	88%
Frontal lobe	3	FPz, FP1, FP2	70%

To investigate the significance of the frontal lobe for classification, a statistical analysis is conducted about the difference in cortical signal characteristics between left and right stepping-based MI tasks for frontal lobe channels. The wavelet energy spectrum of each EEG signal epoch is calculated using the continuous wavelet transform with the mother function of the complex-valued Morlet wavelet [48, 52]. For each frontal lobe channel, the wavelet energy spectra E_L and E_R (associated with left and right stepping-based MI tasks) are calculated by averaging the total spectrum over the indicated frequency band at each experimental session. The paired T-Test results between E_L and E_R in the frontal lobe are displayed in Table 7. The results indicate that the commonly used β band (15-35 Hz) features exhibit no significant differences between the two imaginary movements for FPz, FP1, and FP2. Most θ and μ band features significantly differ between left and right stepping-based MI tasks in both experiments ($\alpha=0.05$), except for the FP2 channel in the μ band. These new findings confirm the substantial contribution of the frontal lobe to stepping-based MI tasks, and provide a basis for further development of cross-subject lower limb BCI systems.

Table 7 The paired T-Test results of channels FPZ, FP1 and FP2

Channels	p-value					
	Saline Electrode			Gel Electrode		
	θ (4-8 Hz)	μ (8-15 Hz)	β (15-35 Hz)	θ (4-8 Hz)	μ (8-15 Hz)	β (15-35 Hz)
FPz	-	-	-	0.02578*	0.03562*	0.73181
FP1	0.02084*	0.04312*	0.89097	0.01732*	0.03714*	0.51141
FP2	0.01731*	0.10143	0.97546	0.03794*	0.11533	0.75326

Note: * represents the significant difference

4. Conclusion

Based on physiological brain functions, this paper has proposed an optimal cross-subject lower limb channel selection to selectively retain significant channels, narrow the computation scope, and obtain the optimal solutions. Experiments with lower limb stepping MI tasks have been conducted using saline and gel electrodes on six able-bodied subjects. The experimental results have demonstrated that the proposed schemes can efficiently classify MI-based EEG data in low-channel settings. Compared to schemes with complicated DTL classifiers, lightweight DTL classifiers (such as the AlexNet) yield the higher classification performance and accuracy. Statistical analysis has revealed that there is a significant difference in energy spectrum between left and right stepping-based MI tasks in the θ and μ bands of frontal lobe channels.

The proposed optimal channel selection solution and the stepping-based MI classification scheme have

addressed the cross-subject channel selection problem for lower limb MI classification, overcome the challenge of limited channel numbers due to inconvenient use, and improved the reusability of data and models. Comparative results on accuracy and time complexity (between various DTL classifiers) have facilitated the construction of high-performance BCIs for stepping-based MI tasks. Notably, manually labeled EEG data is often expensive and time-consuming to collect, clean, and debug. Further work includes adopting an adversarial DTL classifier in the scheme to learn from realistic samples and produce numerous forged samples for training. Additionally, the new findings of significant differences in the energy spectrum (between left and right stepping-based MI tasks) have demonstrated significant impacts of the frontal lobe on lower limb MI tasks. Therefore, the study suggests the potential use of these findings in developing convenient cross-subject lower limb BCI systems for auxiliary and rehabilitation applications.

Author Contributions: **Mingnan Wei:** conceptualization, data curation, formal analysis, investigation, methodology, software, validation, visualization, writing – original draft, writing – review & editing; **Mengjie Huang:** conceptualization, funding acquisition, project administration, resources, supervision, writing – review & editing; **Jiaying Ni:** visualization, writing – original draft, writing – review & editing. All authors have read and agreed to the published version of the manuscript.

Funding: This research is partially supported by: Research Development Fund of Xi'an Jiaotong-Liverpool University (RDF-18-02-30).

Data Availability Statement: Not applicable.

Conflicts of Interest: All authors declare no conflicts of interest in this paper.

Acknowledgment: The authors would like to gratefully acknowledge the support from Prof. Eng Gee Lim and Dr. Mark Leach of Suzhou Municipal Key Laboratory for Broadband Wireless Technologies.

References

- Olsen, S.; Zhang, J.W.; Liang, K.F.; *et al.* An artificial intelligence that increases simulated brain–computer interface performance. *J. Neural Eng.*, **2021**, *18*: 046053.
- Singh, A.; Hussain, A.A.; Lal, S.; *et al.* A comprehensive review on critical issues and possible solutions of motor imagery based electroencephalography brain-computer interface. *Sensors*, **2021**, *21*: 2173.
- Zabcikova, M.; Koudelkova, Z.; Jasek, R.; *et al.* Recent advances and current trends in brain-computer interface research and their applications. *Int. J. Dev. Neurosci.*, **2022**, *82*: 107–123.
- Ahn, M.; Cho, H.; Ahn, S.; *et al.* User's self-prediction of performance in motor imagery brain-computer interface. *Front. Hum. Neurosci.*, **2018**, *12*: 59.
- Leeuwis, N.; Yoon, S.; Alimardani, M. Functional connectivity analysis in motor-imagery brain computer interfaces. *Front. Human Neurosci.*, **2021**, *15*: 732946.
- Wan, Z.T.; Yang, R.; Huang, M.; *et al.* EEG fading data classification based on improved manifold learning with adaptive neighborhood selection. *Neurocomputing*, **2022**, *482*: 186–196.
- Wang, H.T.; Li, T.; Bezerianos, A.; *et al.* The control of a virtual automatic car based on multiple patterns of motor imagery BCI. *Med. Biol. Eng. Comput.*, **2019**, *57*: 299–309.
- Yu, N.X.; Yang, R.; Huang, M.J. Deep common spatial pattern based motor imagery classification with improved objective function. *Int. J. Network Dyn. Intell.*, **2022**, *1*: 73–84.
- Formaggio, E.; Masiero, S.; Bosco, A.; *et al.* Quantitative EEG evaluation during robot-assisted foot movement. *IEEE Trans. Neural Syst. Rehabil. Eng.*, **2016**, *25*: 1633–1640.
- Kline, A.; Ghiroaga, C.G.; Pittman, D.; *et al.* EEG differentiates left and right imagined lower limb movement. *Gait Post.*, **2021**, *84*: 148–154.
- Tariq, M.; Trivailo, P.M.; Simic, M. EEG-based BCI control schemes for lower-limb assistive-robots. *Front. Human Neurosci.*, **2018**, *12*: 312.
- Dai, Y.X.; Wang, X.; Zhang, P.B.; *et al.* Sparsity constrained differential evolution enabled feature-channel-sample hybrid selection for daily-life EEG emotion recognition. *Multimed. Tools Appl.*, **2018**, *77*: 21967–21994.
- Geng, H.; Wang, Z.D.; Chen, Y.; *et al.* Multi-sensor filtering fusion with parametric uncertainties and measurement censoring: Monotonicity and boundedness. *IEEE Trans. Signal Process.*, **2021**, *69*: 5875–5890.
- Li, Q.; Wang, Z.D.; Shen, B.; *et al.* A resilient approach to recursive distributed filtering for multirate systems over sensor networks with time-correlated fading channels. *IEEE Trans. Signal Inf. Process. Over Networks*, **2021**, *7*: 636–647.
- Nakanishi, M.; Wang, Y.T.; Wei, C.S.; *et al.* Facilitating calibration in high-speed BCI spellers via leveraging cross-device shared latent responses. *IEEE Trans. Biomed. Eng.*, **2020**, *67*: 1105–1113.
- Strypsteen, T.; Bertrand, A. End-to-end learnable EEG channel selection for deep neural networks with gumbel-softmax. *J. Neural Eng.*, **2021**, *18*: 0460a9.
- Qi, F.F.; Wu, W.; Yu, Z.L.; *et al.* Spatiotemporal-filtering-based channel selection for single-trial EEG classification. *IEEE Trans. Cybernet.*, **2021**, *51*: 558–567.
- Curve, D.; Delisle-Rodriguez, D.; Romero-Laiseca, M.; *et al.* Subject-specific EEG channel selection using non-negative matrix factorization for lower-limb motor imagery recognition. *J. Neural Eng.*, **2020**, *17*: 026029.
- Gaur, P.; McCreadie, K.; Pachori, R.B.; *et al.* An automatic subject specific channel selection method for enhancing motor imagery

- classification in EEG-BCI using correlation. *Biomed. Signal Process. Control*, **2021**, 68: 102574.
20. Homan, R.W.; Herman, J.; Purdy, P. Cerebral location of international 10–20 system electrode placement. *Electroencephalogr. Clin. Neurophysiol.*, **1987**, 66: 376–382.
 21. Hsu, W.C.; Lin, L.F.; Chou, C.W.; et al. EEG classification of imaginary lower limb stepping movements based on fuzzy support vector machine with kernel-induced membership function. *Int. J. Fuzzy Syst.*, **2017**, 19: 566–579.
 22. Liu, Y.H.; Lin, L.F.; Chou, C.W.; et al. Analysis of electroencephalography event-related desynchronisation and synchronisation induced by lower-limb stepping motor imagery. *J. Med. Biol. Eng.*, **2019**, 39: 54–69.
 23. Brissenden, J.A.; Tobyn, S.M.; Osher, D.E.; et al. Topographic cortico-cerebellar networks revealed by visual attention and working memory. *Curr. Biol.*, **2018**, 28: 3364–3372.e5.
 24. Leisman, G.; Moustafa, A.A.; Shafir, T. Thinking, walking, talking: Integratory motor and cognitive brain function. *Front. Public Health*, **2016**, 4: 94.
 25. Raffin, E.; Mattout, J.; Reilly, K.T.; et al. Disentangling motor execution from motor imagery with the phantom limb. *Brain*, **2012**, 135: 582–595.
 26. Ren, S.X.; Wang, W.Q.; Hou, Z.G.; et al. Enhanced motor imagery based brain-computer interface via FES and VR for lower limbs. *IEEE Trans. Neural Syst. Rehabil. Eng.*, **2020**, 28: 1846–1855.
 27. Brunner, C.; Delorme, A.; Makeig, S. EEGLAB—an open source matlab toolbox for electrophysiological research. *Biomed. Tech.* **2013**, 58 Suppl 1, SI-1-Track-G, 000010151520134182. doi: [10.1515/bmt-2013-4182](https://doi.org/10.1515/bmt-2013-4182)
 28. Geng, H.; Liu, H.J.; Ma, L.F.; et al. Multi-sensor filtering fusion meets censored measurements under a constrained network environment: Advances, challenges and prospects. *Int. J. Syst. Sci.*, **2021**, 52: 3410–3436.
 29. Mao, J.Y.; Sun, Y.; Yi, X.J.; et al. Recursive filtering of networked nonlinear systems: A survey. *Int. J. Syst. Sci.*, **2021**, 52: 1110–1128.
 30. Debener, S.; Thorne, J.; Schneider, T.R.; et al. Using ICA for the analysis of multi-channel EEG data. In *Simultaneous EEG and fMRI: Recording, Analysis, and Application*; Ullsperger, M.; Debener, S., Eds.; Oxford University Press: Oxford, 2010; pp. 121–134.
 31. He, H.; Wu, D.R. Transfer learning for brain–computer interfaces: A Euclidean space data alignment approach. *IEEE Trans. Biomed. Eng.*, **2020**, 67: 399–410.
 32. Yang, B.H.; He, M.Y.; Liu, Y.Y.; et al. Multi-class feature extraction based on common spatial patterns of multi-band cross filter in BCIs. In *International Computer Science Conference, Shanghai, China, 27–30 October 2012*; Springer: Berlin/Heidelberg, Germany, 2012; pp. 399–408. doi: [10.1007/978-3-642-34381-0_46](https://doi.org/10.1007/978-3-642-34381-0_46)
 33. Tan, C.Q.; Sun, F.C.; Kong, T.; et al. A survey on deep transfer learning. In *27th International Conference on Artificial Neural Networks, Rhodes, Greece, 4–7 October, 2018*; Springer: Berlin/Heidelberg, Germany, 2018; pp. 270–279. doi: [10.1007/978-3-030-01424-7_27](https://doi.org/10.1007/978-3-030-01424-7_27)
 34. Tan, C.Q.; Sun, F.C.; Zhang, W.C. Deep transfer learning for EEG-based brain computer interface. In *2018 IEEE International Conference on Acoustics, Speech and Signal Processing (ICASSP), Calgary, AB, Canada, 15–20 April 2018*; IEEE: New York, 2018; pp. 916–920. doi: [10.1109/ICASSP.2018.8462115](https://doi.org/10.1109/ICASSP.2018.8462115)
 35. Völker, M.; Schirrmester, R.T.; Fiederer, L.D.J.; et al. Deep transfer learning for error decoding from non-invasive EEG. In *2018 6th International Conference on Brain-Computer Interface (BCI), Gangwon, Korea (South), 15–17 January 2018*; IEEE: New York, 2018; pp. 1–6. doi: [10.1109/IWW-BCI.2018.8311491](https://doi.org/10.1109/IWW-BCI.2018.8311491)
 36. Wan, Z.T.; Yang, R.; Huang, M.J.; et al. A review on transfer learning in EEG signal analysis. *Neurocomputing*, **2021**, 421: 1–14.
 37. Zhao, G.Y.; Li, Y.T.; Xu, Q.R. From emotion AI to cognitive AI. *Int. J. Network Dyn. Intell.*, **2022**, 1: 65–72.
 38. Deepak, S.; Ameer, P.M. Brain tumor classification using deep CNN features via transfer learning. *Comput. Biol. Med.*, **2019**, 111: 103345.
 39. Pahar, M.; Klopper, M.; Warren, R.; et al. COVID-19 detection in cough, breath and speech using deep transfer learning and bottleneck features. *Comput. Biol. Med.*, **2022**, 141: 105153.
 40. Wang, C.; Wang, Z.D.; Liu, W.B.; et al. A novel deep offline-to-online transfer learning framework for pipeline leakage detection with small samples. *IEEE Trans. Instrum. Meas.*, **2022**, 72: 3503913.
 41. Dehghani, M.; Mobaeni, A.; Boostani, R. A deep neural network-based transfer learning to enhance the performance and learning speed of BCI systems. *Brain-Comput. Interfaces*, **2021**, 8: 14–25.
 42. Lu, B.; Song, B.Y.; Xu, L. Human face recognition based on convolutional neural network and augmented dataset. *Syst. Sci. Control Eng.*, **2021**, 9: 29–37.
 43. Wang, X.Y.; Yang, R.; Huang, M.J. An unsupervised deep-transfer-learning-based motor imagery EEG classification scheme for brain–computer interface. *Sensors*, **2022**, 22: 2241.
 44. Zeng, N.Y.; Wang, Z.D.; Zhang, H.; et al. An improved particle filter with a novel hybrid proposal distribution for quantitative analysis of gold immunochromatographic strips. *IEEE Trans. Nanotechnol.*, **2019**, 18: 819–829.
 45. Zhang, B.C.; Wang, W.N.; Xiao, Y.T.; et al. Cross-subject seizure detection in EEGs using deep transfer learning. *Comput. Math. Methods Med.*, **2020**, 2020: 7902072.
 46. Bagherzadeh, S.; Shahabi, M.S.; Shalhaf, A. Detection of schizophrenia using hybrid of deep learning and brain effective connectivity image from electroencephalogram signal. *Comput. Biol. Med.*, **2022**, 146: 105570.
 47. Ding, Y.L.; Fu, M.H.; Luo, P.; et al. Network learning for biomarker discovery. *Int. J. Network Dyn. Intell.*, **2023**, 2: 51–65.
 48. Khademi, Z.; Ebrahimi, F.; Kordy, H.M. A transfer learning-based CNN and LSTM hybrid deep learning model to classify motor imagery EEG signals. *Comput. Biol. Med.*, **2022**, 143: 105288.
 49. Li, X.; Li, M.L.; Yan, P.F.; et al. Deep learning attention mechanism in medical image analysis: Basics and beyonds. *Int. J. Network Dyn. Intell.*, **2023**, 2: 93–116.
 50. Shakiba, F.M.; Shojae, M.; Azizi, S.M.; et al. Real-time sensing and fault diagnosis for transmission lines. *Int. J. Network Dyn. Intell.*, **2022**, 1: 36–47.
 51. Alicja, M.; Maciej, S. Can AI see bias in X-ray images. *Int. J. Network Dyn. Intell.*, **2022**, 1: 48–64.
 52. Wei, M.N.; Yang, R.; Huang, M.J. Motor imagery EEG signal classification based on deep transfer learning. In *2021 IEEE 34th International Symposium on Computer-Based Medical Systems (CBMS), Aveiro, Portugal, 7–9 June 2021*; IEEE: New York, 2021; pp. 85–90. doi: [10.1109/CBMS52027.2021.00083](https://doi.org/10.1109/CBMS52027.2021.00083)
 53. Cheng, H.J.; Wang, Z.D.; Wei, Z.H.; et al. On adaptive learning framework for deep weighted sparse autoencoder: A multiobjective evolutionary algorithm. *IEEE Trans. Cybern.*, **2020**, 52: 3221–3231.
 54. Liang, C.M.; Li, Y.W.; Liu, Y.H.; et al. Segmentation and weight prediction of grape ear based on SFNet-ResNet18. *Syst. Sci. Con-*

- trol Eng.*, **2022**, *10*: 722–732.
55. Morid, M.A.; Borjali, A.; Del Fiol, G. A scoping review of transfer learning research on medical image analysis using ImageNet. *Comput. Biol. Med.*, **2021**, *128*: 104115.
56. Sun, J.Y.; Wang, Z.D.; Yu, H.; *et al.* Two-stage deep regression enhanced depth estimation from a single RGB image. *IEEE Trans. Emerg. Top. Comput.*, **2022**, *10*: 719–727.

Citation: Wei, M.; Huang, M.; Ni, J. Cross-Subject EEG Channel Selection Method for Lower Limb Brain-Computer Interface. *International Journal of Network Dynamics and Intelligence*. 2023, 2(3), 100008. doi: [10.53941/ijndi.2023.100008](https://doi.org/10.53941/ijndi.2023.100008)

Publisher’s Note: Scilight stays neutral with regard to jurisdictional claims in published maps and institutional affiliations.



Copyright: © 2023 by the authors. This is an open access article under the terms and conditions of the Creative Commons Attribution (CC BY) license <https://creativecommons.org/licenses/by/4.0/>.